Sulphur storage in cold molecular clouds: the case of the $NH_4^+SH^-$ salt on interstellar dust grains

J. Vitorino [1]★ J.-C. Loison [2] V. Wakelam [3] E. Congiu [1] and F. Dulieu [1]★

[1]*CY Cergy Paris Université, Observatoire de Paris, PSL Research University, CNRS, LERMA, F-95000 Cergy, France*
[2]*Université de Bordeaux, Institut des Sciences Moléculaires, UMR 5255, F-33400 Talence, France*
[3]*Laboratoire d'Astrophysique de Bordeaux, Université de Bordeaux, CNRS, B18N, allée Geoffroy Saint-Hilaire, F-33615 Pessac, France*

ABSTRACT

In comets and in the cold phase of the interstellar medium (ISM), ammonium salts are key molecular species due to their role in the retention of volatile compounds on cold surfaces. In the case of sulphur, the H_2S/OCS ratio observed in protostars could be explained by the presence of ammonium hydrosulphide (NH_4SH) salts. However, laboratory data on the properties of NH4SH in ISM cold relevant conditions are rather scarce, as they usually focus on the atmosphere of Jupiter. We propose to consolidate the laboratory data regarding NH_4SH on grains, by performing temperature programmed desorption experiments and Fourier transform infrared reflection spectroscopy. The salt was also exposed to H atoms to mimic the ISM conditions. NH_4SH was found to form *in situ* at 10 K, from a mixture of ammonia (NH_3) and hydrogen sulphide (H_2S). The NH_4^+ infrared feature ($1485\,cm^{-1}$) is the most prominent one at 80 K. As pure species, H_2S and NH_3 desorb at 76 and 90 K, respectively, whereas they are released into the gas phase at 153 K when adsorbed in the form of salt. The presence of water delays the desorption of the salt until the very end of the water desorption, but does not affect the desorption kinetics. During H-exposure, the salt is dissociated and no new product was detected. As a comparative study, salts have been included in the Nautilus gas–grain model. The results show a good correlation with the observations of IRAS 16293−2422B, as opposed to when NH_4SH is not included in the model.

Key words: astrochemistry – molecular processes – methods: laboratory: solid state – ISM: clouds – ISM: molecules.

1 INTRODUCTION

Laboratory data about ammonium hydrosulfide ($NH_4^+SH^-$, hereafter NH_4SH) characteristics in interstellar medium (ISM) relevant conditions are rather scarce. Indeed, in terrestrial conditions, ammonium hydrosulfide is known to be formed via the mixing of gaseous hydrogen sulfide (H_2S) and ammonia (NH_3), which are corrosive chemical compounds with high toxicity for humans. Additionally, their use asks for a very precise leak control, especially for H_2S, given the intense odour detectable by smell well before the recommended exposure limit concentration.[1] NH_4SH is one of the most interesting salts potentially present in the ISM and in the upper layer of the coma in comets such as 67P/Churyumov–Gerasimenko (Altwegg et al. 2020). The detection of sulphur and ammonia clouds in overlapping layers by the Galileo probe on Jupiter, with a uniform mixture at 10 bars, also indicates that NH_4SH is a major compound of gas-giant planets atmosphere (Niemann et al. 1998; Pater et al. 2001; Wong et al. 2004; Li et al. 2020). This has been supported by theoretical models (Weidenschilling & Lewis 1973; Atreya et al. 1999; Friedson 2005), as well as spacecraft observations (Roman, Banfield & Gierasch 2013). Consequently, most laboratory

studies investigate the radiolysis and photodissociation of ammonium hydrosulfide. For example, the infrared and radiolytic data produced by Loeffler et al. (2015), allow them to predict that NH_4SH would be detectable mostly in crystalline form at 200 K in gas-giant clouds, but that ionizing radiations would destroy the crystalline structure, producing an amorphous mixture instead. The first documented laboratory experiments of ultraviolet (UV)-photolysis of mixed H_2S, NH_3, and H_2O ices and pure NH_4SH were done by Lebofsky & Fegley (1976), in order to compare the spectra obtained with the observations of Jupiter and Saturn satellites, as well as Saturn rings. More recently, combined studies of UV–vis reflectance spectra of photolyzed NH_4SH, together with visible light imaging of these mixtures, have proven their usefulness for remote sensing campaigns on Jupiter, showing a colour-dependence on the irradiation dose and temperature (Loeffler et al. 2016; Loeffler & Hudson 2018).

Salts are ionic compounds, often formed by proton transfer in an acid–base reaction. The latter can take place at cryogenic temperatures due to a very low-activation energy (Theulé et al. 2013), while the salt created is usually much more refractory than any of the individual species involved in the ionic bond. For instance, NH_3 and HCOOH or CH_3COOH, when interacting in form of ammonium formate ($NH_4^+COO^-$) or ammonium acetate ($NH_4^+CH_3COO^-$), can remain on dust grains far beyond their respective desorption temperature (Bergner et al. 2016; Kruczkiewicz et al. 2021). The same goes for reactions such as $NH_3 + HCN \rightarrow NH_4^+CN^-$ (ammonium cyanide, Clutter & Thompson 1969; Gerakines, Moore &

★ E-mail: julie.vitorino@cyu.fr (JV); francois.dulieu@cyu.fr (FD)
[1]Hydrogen sulfide; SDS No. 295 442 [Print]; Merck Life Science S.A.S.: Saint-Quentin-Fallavier, France, 2024 Jan 3. https://www.sigmaaldrich.com/FR/fr/product/aldrich/295442 (accessed 2024 Mar 4).

Hudson 2004; Noble et al. 2013; Gerakines, Yarnall & Hudson 2024), or $NH_3 + HNCO \rightarrow NH_4^+OCN^-$ (ammonium isocyanate, Demyk et al. 1998; Raunier et al. 2003; Van Broekhuizen, Keane & Schutte 2004). In each of these cases, the reactants are relatively volatile compounds, likely to sublimate from dust grains at comparatively low temperatures (i.e. <100 K for the smallest ones, <200 K for the largest ones). On the other hand, the salts formed sublimate at higher temperatures, allowing the snowline of both volatile species involved in the mixtures to be extended towards warmer regions. Therefore, salts are considered good candidates to be involved in the complexation of early chemistry.

In addition, salts would provide an explanation for some of the most significant depletions in the Universe. For example, a nitrogen depletion is observed in several environments including comets (Filacchione et al. 2019) and ISM (Savage & Sembach 1996), compared to the Solar System ratios (Lodders 2010). Likewise, sulphur is reported missing especially in dense cores and protostellar environments (Tieftrunk et al. 1994; Goicoechea et al. 2006). The abundance of S-bearing species is then approximately 1000 times lower than that found in diffuse clouds (Kushwahaa et al. 2023), which is also not in tone with their abundance in comets (Calmonte et al. 2016; López-Gallifa et al. 2024). So far, there is not one clear explanation to these depletions. Regarding sulphur, it is believed to be trapped in the dust grains cores (Perrero et al. 2024), or in the icy mantles in the form of salts. The latter hypothesis would explain the release of S-containing compounds in comets and enable their detection in larger amounts.

Moreover, the H_2S presence in the early stages of pre-stellar cores development is a determining factor when it comes to understanding the carbonyl sulphide (OCS) as well as the S-bearing molecules content, especially in low-mass stars. The H_2S on interstellar dust grains would indeed be converted to OCS throughout the collapse phase, as long as the core environment is cold enough (typically <20 K) to maintain a high quantity of CO ice (Drozdovskaya et al. 2018). The transformation would mostly happen via grain-surface processes (Ferrante et al. 2008; El Akel et al. 2022). More elaborately, the rate of UV radiations in the pre-stellar core is also likely to determine the fluency of the conversion of H_2S to OCS, as shown by laboratory experiments where a high UV irradiation involves a high conversion rate (Chen et al. 2015), and observations of IRAS $16293-2422$ B, where such a rate would explain the amount and diversity of S-bearing molecules detected compared to the Solar system ratios (Ruffle et al. 1999; Jiménez-Escobar, Caro & Chen 2014; Martín-Doménech et al. 2016; Drozdovskaya et al. 2018; Phuong et al. 2018).

It is thus also necessary to take ammonium salts into account in gas-grain models of protostars, as they would significantly influence the proportion of sulphur available to create S-bearing molecules, despite the apparent depletion.

In this paper, we aim to investigate the nature of the products upon the desorption of NH_4SH. We propose to densify the laboratory data on the formation, infrared (IR) signatures, and characteristics of the salt on a cold surface representing an interstellar dust grain. We performed experiments and analyses with varying ratios of incoming NH_3 and H_2S in pure form, on a bare gold-plated surface, and in the case of a water ice substrate. The reactivity and destruction of the salt under H atoms exposure were also studied. Hereafter, Section 2 describes the experimental methods and setup reproducing the interstellar conditions. In Section 3, we present our infrared spectroscopy and mass spectrometry data on ices of NH_3 and H_2S, on NH_4SH salt, on NH_4SH exposed to H atoms, and finally in the case of mixtures containing water molecules in different proportions.

In Section 4, we discuss the astrophysical implications and show that the inclusion of NH_4SH in a gas grain model can better explain the OCS/H_2S ratio observed towards protostars.

2 EXPERIMENTAL METHODS

All of the experiments have been performed with the VErs de NoUvelles Synthèses (VENUS) experimental setup, located in LERMA-CY and described in detail elsewhere (Congiu et al. 2020). It consists of a gold-coated circular surface of 9 mm diameter, mounted on a closed-cycle He cryostat and held inside an Ultra-High Vacuum stainless steel chamber. The base pressure is approximately of 10^{-10} mbar. Chemical species under a gaseous, liquid, or solid state at room temperature are kept or converted into gas state in the molecular or atomic beamlines, then sent towards the surface by means of a differential pumping through two intermediate chambers. The beams meet on the surface and the gas-phase interactions above the cold sample are negligible. Indeed, the partial pressure does not exceed 10^{-8} mbar in the volume of the beams, and the main chamber is maintained at 10^{-10} mbar even when species are being deposited. The only exception is for H_2 diffusion when the atomic hydrogen beam is being used (the partial pressure of the chamber therefore going up to 10^{-8} mbar). Overall, surface–surface and possibly gas-surface interactions are largely dominant compared to gas–gas interactions. Representing an interstellar dust grain, the surface temperature can vary between 6 and 350 K and is computer-controlled by means of a resistive heater clamped behind the sample holder.

2.1 RAIRS and TPD

A typical experiment consists of two phases. The species are deposited at a constant temperature for a sufficiently long time to allow their detection, forming an ice film on the surface (phase 1, deposition), before being sublimated and released in gaseous form during a linear increase in the temperature of the surface (phase 2, temperature programmed desorption, TPD). During both phases, we can monitor the ice evolution with a Vertex-70 Fourier Transform infrared (FT-IR) spectrometer, performing reflection absorption infrared spectroscopy (RAIRS), a non-destructive analysis technique. The surface is continuously scanned with a grazing infrared beam at an $83°$ angle, over a spectral range of $800-4500$ cm^{-1} (12.5–2.22 µm). The light coming from the sample with the desired angle is collected in a N_2-cooled mercury cadmium telluride (MCT) detector. Every two minutes (corresponding to 256 scans), a mean spectrum is produced.

Once the deposition at low temperature is achieved, the temperature of the surface is linearly increased at a rate $\beta = 0.2$ K s^{-1}. The desorbing species are detected with a Hiden 51/3F vertically translatable quadrupole mass spectrometer (QMS), placed 5 mm in front of the surface during the course of the TPD. Every molecule and fragment can then be probed according to their respective mass, chosen by the user and measured in atomic mass units (amu). The ionization energy of the QMS was set at 30 eV, and the number of species entering the QMS head is monitored as a function of temperature. From this, numerous parameters can be derived, including the binding energies between the molecules and the gold surface.

2.2 Atomic, water, and molecular beams

In this work we have carried out a series of experiments, as shown in Table 1, for which we provide TPD and infrared data. They can be grouped into several categories: individual species (i, ii),

Table 1. List of the conducted experiments and their associated parameters (composition of the ice, coverage, deposition temperature, and H flux when used).

Exp.	Reactive system	Coverage (monolayers)	T_{dep} (K)	H flux (atoms cm^{-2} s^{-1})
i	{H$_2$S}	0.1; 0.15; 0.35; 0.65	10	–
ii	{NH$_3$}	0.35; 0.4; 0.5; 1	10	–
iii	{H$_2$S + H}	0.65 : 10	10	8×10^{12}
iv	{H$_2$S + NH$_3$}	1.8 : 4.65	10	–
v	{H$_2$S + NH$_3$}	1.8 : 1.9	10	–
vi	{H$_2$S + NH$_3$} + {H}	1.8 : 1.9; 50	80; 10	8×10^{12}
vii	{H$_2$S + NH$_3$ + H}	1.8 : 1.9 : 30	10	8×10^{12}
viii	{H$_2$S + NH$_3$ + H$_2$O}	1.9 : 1.9 : 12	10	–
ix	{H$_2$S + NH$_3$ + H$_2$O}	0.8 : 1.5 : 30	10	–
x	{NH$_3$ + H$_2$O}	1 : 6	10	–
xi	{H$_2$S + NH$_3$ + H$_2$O + H}	1.9 : 1.9 : 12 : 30	10	8×10^{12}

hydrogenation of H$_2$S (iii), salt formation (iv, v), salt with H atoms exposure (vi, vii), salt in a water ice matrix (viii, ix), NH$_3$ with water (x), and salt in a water ice matrix and under H-exposure (xi). When two or more species are deposited on the surface, we denote the codeposition by placing all the species in a pair of curly brackets. For instance, in the figures of this paper, we use the notation {$A + B$}$^T_{doseA:doseB}$ to refer to a codeposition of species A and B on the surface, at temperature T, with estimated or calculated doses for each species. Conversely, a sequential deposition is indicated by a series of brackets, that is {$A + B$}$^{T_{AB}}_{doseA:doseB}$ + {C}$^{T_C}_{doseC}$.

The molecular NH$_3$ beam was calibrated as described in Noble et al. (2011). A monolayer (ML), which defines the theoretical filling of all available adsorption sites on the sample and corresponds to $\sim 10^{15}$ molecules cm^{-2}, was reached after 10 and 31 min of deposition, for NH$_3$ and H$_2$S, respectively. This gives corresponding condensation rates – or fluxes – of $\phi_{NH_3} = 1.7 \times 10^{12}$ molecules cm^{-2} s^{-1}, and $\phi_{H_2S} = 5.4 \times 10^{11}$ molecules cm^{-2} s^{-1}. On the other hand, in the case of H$_2$O, water vapour was leaked into the main chamber via a delivery manifold with known characteristics (a monolayer grown in approximately 5 min, giving $\phi_{H_2O} = 3.3 \times 10^{12}$ molecules cm^{-2} s^{-1}). For water, the thickness of an ice layer of 1 ML is 3 Å, which is also a good estimate for other species of comparable size.

In the case of hydrogen, only H$_2$ molecules can be stored in a gas bottle. The atoms were obtained by dissociating the molecules and creating a plasma in a quartz tube surrounded by a microwave cavity (Surfatron). The H atoms have a short residence time on one adsorption site, due to their propensity to diffuse and recombine rapidly to form H$_2$. Therefore, their quantity in ML can only be estimated with the maximum number of reactions that can occur in a barrierless reaction such as NO + H (Congiu et al. 2012). One 'monolayer' of H atoms is then considered to be achieved in about 2 min when the flux is of $\phi_H = 8 \times 10^{12}$ atoms cm^{-2} s^{-1}. The H$_2$ dissociation efficiency was measured before each experiment with H atoms, giving an average of $\sim$62 per cent, with a possible variation of at most 20 per cent between two different experiments.

3 RESULTS

3.1 Single-component ices: NH$_3$ and H$_2$S depositions

A characterization of the individual species was first carried out in order to determine their properties under our experimental conditions. Fig. 1 displays the TPD spectra of 0.6 monolayers of H$_2$S, and 1 monolayer of NH$_3$. Both species were deposited at 10 K and desorb from the surface at 76 and 90 K respectively, following a first order desorption behaviour. Several fragments can be identified for each
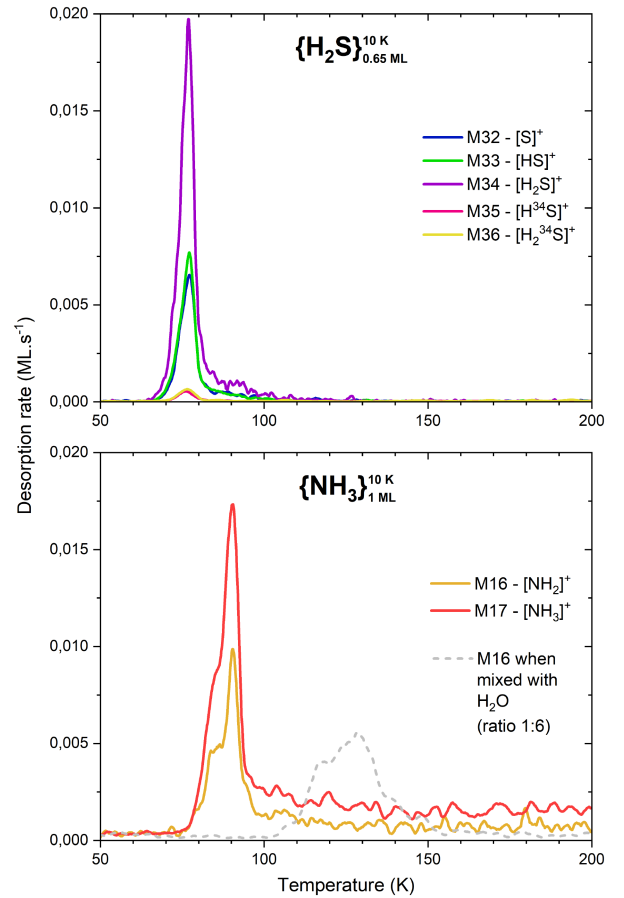

Figure 1. TPD spectra of 0.65 monolayers of H$_2$S (top panel), and of 1 monolayer of NH$_3$ (bottom panel). Both species were deposited at 10 K. Each curve represents a fragment ionized by the QMS. The dotted line stands for $m/z = 16$ when NH$_3$ is mixed with H$_2$O.

species, as shown with each curve, giving a unique cracking pattern for each molecule (see upper panel of Fig. 2). The amounts of each fragment depend mainly on the ionization energy of the QMS, which in this work was set at 30 eV. The H$_2$S and NH$_3$ major fragments correspond to the ionized unimpaired molecules: $m/z = 34$ for H$_2$S$^+$ and $m/z = 17$ for NH$_3^+$.

In the case of H$_2$S, we detect between 3 and 4 per cent of ^{34}S, an amount that is not considered to significantly affect the nature and kinetics of the reactions with H and NH$_3$. Even when less than 1
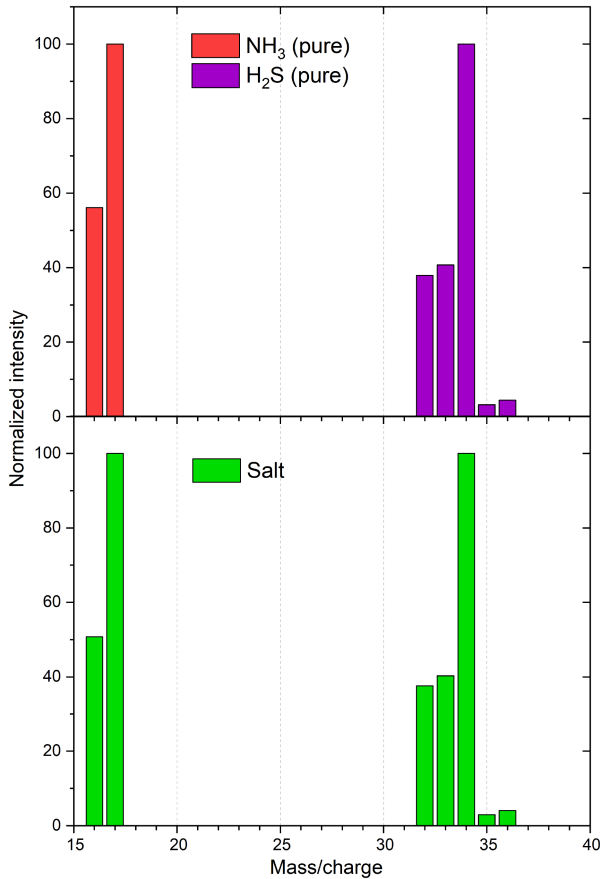
Figure 2. Mass spectra of NH₃ (top left), H₂S (top right), and NH₄SH (bottom). The intensities have been normalized to the most abundant fragment for each of the pure species (m/z = 17 for NH₃, m/z = 34 for H₂S). For NH₄SH, the ammonium fragments are normalized to mass 17, while the hydrogen sulfide fragments are normalized to mass 34.

ML of H₂S is deposited on the sample, the molecules quickly exhibit a multilayer behaviour under our conditions, making it difficult to determine the time after which a monolayer is reached. Moreover, the areas under the main fragment curves of both H₂S and NH₃ are not directly comparable to each other due to their different ionization cross-sections at 30 eV, of respectively $\sigma_{H_2S}^{tot}$ = 3.18 Å² (Vinodkumar et al. 2011) and $\sigma_{NH_3}^{tot}$ = 1.57 Å² (Kumar & Kumar 2020), giving a ratio of $\frac{\sigma_{H_2S}}{\sigma_{NH_3}} \sim 2.02$. Consequently, the determination of the monolayer completion for H₂S (31 min) was based on the value obtained for NH₃ (10 min). Measurements in the salt (cf. Section 3.2) further confirm a calculated ratio of ~1.9 between the two species, which is in good agreement with the total cross-sections found in the literature.

The infrared bands of H₂S and NH₃ are shown in Fig. 3 with asterisks (∗), and the values are listed in Table 2. When very little product is present on the surface, the only relevant and usable signature of H₂S is a small absorption band at 2570 cm⁻¹, testifying to the HS⁻ stretching mode (ν_3), in agreement with other studies (Jiménez-Escobar et al. 2014; Loeffler et al. 2015; Oba et al. 2018). The detection of H₂S with a grazing infrared beam is rather difficult, due to the very broad nature of its main signature and to the associated low-band strength, determined directly from experimental measurements at A(S–H) = 1.12 × 10⁻¹⁷ cm molecule⁻¹ (Hudson & Gerakines 2018). Ammonia infrared signatures are present at 3380
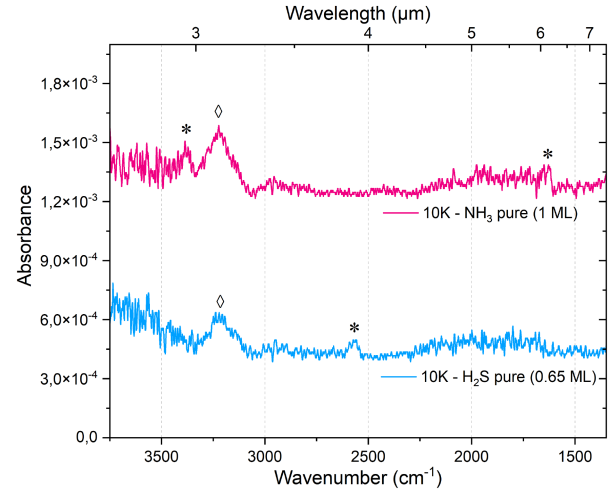

Figure 3. Infrared spectra of 0.65 monolayers of H₂S (bottom curve) and of 1 monolayer of NH₃ (top curve). The species signatures are shown with ∗, while the diamonds (◊) indicate residual water present on the detector window, that has not been deposited on the surface.

and 1642 cm⁻¹ (ν_3 and ν_4 NH bending modes of NH₃). They also correspond to the known features documented in the literature (Gálvez et al. 2010; Kruczkiewicz et al. 2021). On both spectra, as well as in the other spectra presented in this work, the broad, sharp absorption band at 3205 cm⁻¹, indicated by diamonds (◊), is due to residual water condensed on the IR detector window.

3.2 Salt formation: H2S:NH3 mixtures

When mixed together, ammonia and hydrogen sulfide interact to form ammonium hydrosulfide. Fig. 4 shows the TPD results of experiment (iv) on the left panel, and of experiment (v) on the right panel. In both cases, NH₃ and H₂S gases were codeposited on the surface held at 10 K, via two different molecular beams. In (iv), NH₃ was in excess (4.65 ML) compared to H₂S (1.8 ML), while in (v) both formed an ~1:1 mixture, (1.9 ML of NH₃ with 1.8 ML of H₂S). Only the desorption curves of the major fragments resulting from the temperature increase are shown. The absence of signal for the m/z = 51 confirms that, being a salt, NH₄SH is an electrovalent compound and does not contain any covalent bond forming a molecule, but rather two ions HS⁻ and NH₄⁺ (Bragin et al. 1977; Loeffler et al. 2015). This is the case for many salts (Raunier et al. 2003; Noble et al. 2013; Kruczkiewicz et al. 2021; Gerakines et al. 2024). Therefore, we observe m/z = 34 and m/z = 17 as the main components of the salt, desorbing at 153 and 154 K in the two experiments. With very little desorption of pure molecular H₂S and NH₃, we note that 6 per cent and 18 per cent of H₂S remain pure in the exp. (iv) and (v) respectively, while 17 per cent and 14 per cent of NH₃ remain pure in exp. (iv) and (v), respectively. These results, together with those shown before in Fig. 2, confirm the protection of both NH₃ and H₂S against the temperature increase. They are stored in salt form at temperatures at which the volatile species would already have desorbed, only to be released in their original form during the sublimation. This behaviour is however not unique to NH₄SH; most salts tend to dissociate into two more volatile species, when facing a sufficient temperature increase (Noble et al. 2013; Kruczkiewicz et al. 2021; Gerakines et al. 2024).

By calculating the ratio between two representative masses of a chemical species, it is possible to evaluate its conservation in the

Table 2. List of infrared features observed in our experiments and found in the literature. [a](Smith 1991), [b](Oba et al. 2018), [c](Kruczkiewicz et al. 2021), [d](Gálvez et al. 2010), [e](Ferraro, Sill & Fink 1980), [f](Bragin et al. 1977), [g](Hudson & Gerakines 2018), [h](Fathe et al. 2006), [i](Loeffler et al. 2015), [j](d'Hedencourt & Allamandola 1986), [k](Bouilloud et al. 2015), [l](Hudgins et al. 1993).

| Experiment | Exp. no. | H$_2$S | | NH$_3$ | | NH$_4$SH | | | H$_2$O | |
| | | | | | | NH$_4^+$ | | HS$^-$ | | |
		ν_1[a]	ν_3[a,b,g,h]	ν_3[c,d]	ν_4[c,d]	ν_4[c,d,i]	ν_3[e]	ν_4[e,f]	ν_1[l]	ν_2[j,k]
{H$_2$S}	i	–	2568	–	–	–	–	–	–	–
{NH$_3$}	ii	–	–	3383	1642	–	–	–	–	–
{H$_2$S + NH$_3$}	iv	–	–	3364	1631	1488	3007	1814	–	–
	v	–	2567	3371	1631	1483	–	–	–	–
{H$_2$S + NH$_3$} + {H}	vi	–	–	3371	–	1475	3007	–	–	–
{H$_2$S + NH$_3$ + H}	vii	–	2572	3366	1628	1480	3003	–	–	–
{H$_2$S + NH$_3$ + H$_2$O}	viii	–	2554	3390	1641	1478	–	–	3312	1684
	ix	2527	–	3385	1644	1487	–	–	3336	1681
{NH$_3$ + H$_2$O}	x	–	–	3398	1643	–	–	–	3341	1690
{H$_2$S + NH$_3$ + H$_2$O + H}	xi	–	2551	3388	1643	1478	3009	–	3310	1681
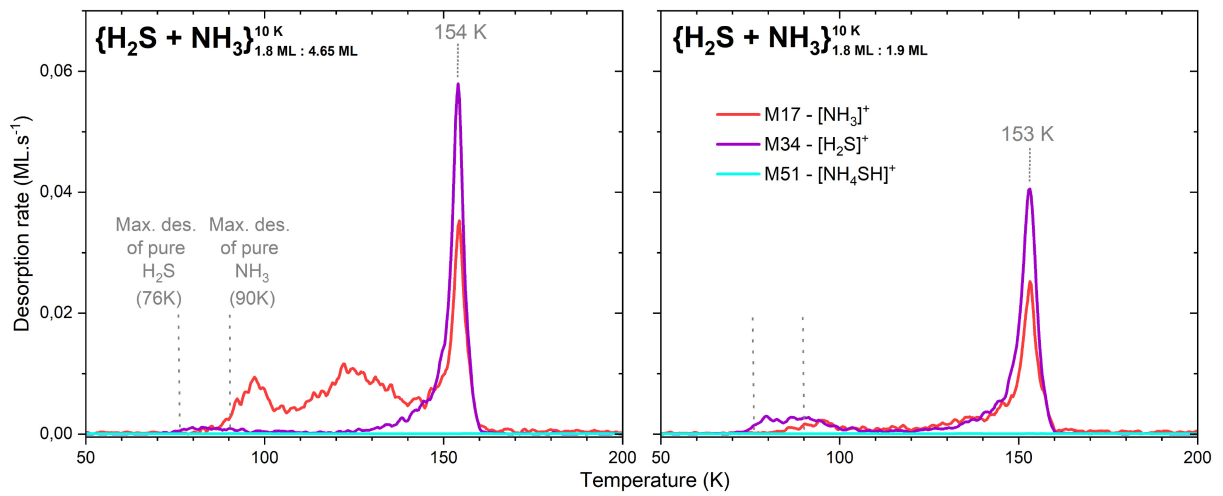
Figure 4. TPD spectra of H$_2$S:NH$_3$ mixtures. The left panel shows results of the experiment (iv), where NH$_3$ was more abundant than H$_2$S on the surface. The right panel shows the results of the experiment (v), where NH$_3$ and H$_2$S formed a homogeneous mixture on the surface. Only the major fragments are shown. The grey dotted lines indicate the temperatures at which each product desorbs in its pure form.

final detection by the QMS. In fact, with a fixed cracking pattern and non-varying experimental conditions, the ratio between each of the fragments is supposed to remain identical. However, if a reaction involving a different species produces a new product, the latter will have different binding, cohesive, and interaction energies, thus altering the proportions between the masses. To determine whether the salt desorbs as an independent entity (namely a hypothetical molecular NH$_4$SH) or breaks down into two pure species, we calculated the ratios between $m/z = 33$ and 34 for H$_2$S, and $m/z = 16$ and 17 for NH$_3$. The values are reported in Table 3. We find that the 33/34 ratio is not different in pure H$_2$S or in the salt, being constant at ∼0.4. The 16/17 ratio is slightly different when calculated from a TPD of purely NH$_3$ or of salt (∼0.55 and ∼0.5, respectively). However, the total ratio remains in the same range, indicating the dissociation of the salt into two different species.

In the experiment with an excess of NH$_3$ (iv), there is also a peculiar desorption of $m/z = 17$ between 90 and 142 K, with a maximum at 117 K. It represents 46 per cent of the total ammonia sent on the surface during this experiment. Ammonia ice alone shows a peak at 90 K, but if it is likely to form H-bonds with other components on the surface, especially with water, its desorption is delayed towards higher temperatures, as shown by the dashed grey line of Fig. 1

Table 3. Proportions between different m/z ratios in individual species and in the salt.

Experiment	33/34	16/17
{H$_2$S} (i)	0.41	–
{NH$_3$} (ii)	–	0.56
{H$_2$S + H} (iii)	0.41	–
{H$_2$S + NH$_3$} – excess of NH$_3$ (iv)	0.41	0.51
{H$_2$S + NH$_3$} – homog. mixture (v)	0.40	0.48
{H$_2$S + NH$_3$} + {H} (vi)	0.41	0.57
{H$_2$S + NH$_3$ + H$_2$O} (viii)	0.40	–
{H$_2$S + NH$_3$ + H$_2$O} (ix)	0.39	–

(lower panel) (Suresh et al. 2024). In the case where ammonia is mixed with H$_2$S, we believe that the same mechanism occurs between NH$_3$ and the salt. The cracking pattern of ammonia is preserved, suggesting that it is not chemically bonded to any compound, but is only slightly interacting with NH$_4$SH. We refer to these molecules as 'interacting NH$_3$', as opposed to 'non-interacting NH$_3$', which characterizes molecules that do not interact with the salt. We also note that some of the 'non-interacting NH$_3$' could be related to the
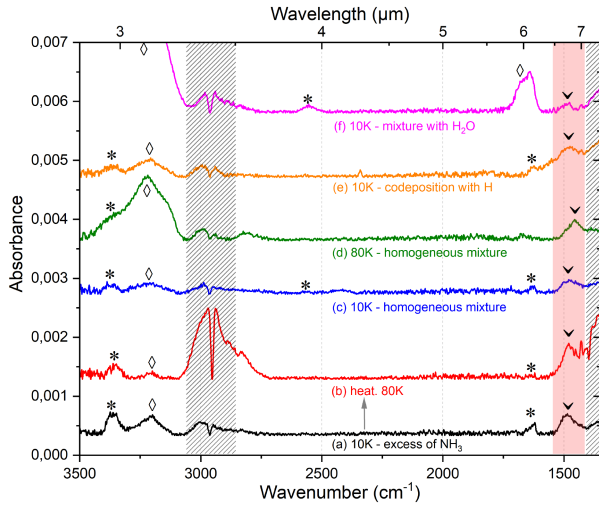
Figure 5. Infrared spectra for the main experiments. *a, c, d, e, f* correspond to experiments iv, v, vi, vii, viii. The spectrum *b* was recorded at 80 K, during the heating phase after the deposition of {H₂S + NH₃} (iv). The spectrum *d* was recorded at 80 K, before the H bombardment phase of the salt (experiment vi). The arrows ∨ indicate the salt signature and the symbol ∗ denotes the signatures of pure H₂S and NH₃. The symbol ◇ indicates the bands of H₂O, whether caused by ice condensed on the MCT detector window (*a, b, c, d*), or ice intentionally deposited on the surface (*f*), or condensed on the surface due to residual pressure of H₂O in the main chamber (*d*).

uneven coverage between the two beams used to mix NH₃ and H₂S. However, this amount should not exceed 10 per cent.

In the mid-IR region, NH₄SH has visible spectral signatures. The spectra associated with simple H₂S:NH₃ mixtures (experiments iv, v, and first phase of vi), correspond to the curves *a, c,* and *d* in Fig. 5. The absorption bands and corresponding wavenumbers are listed in Table 2. Already at 10 K, the most prominent feature observed in all NH₄SH experiments performed in this work is the ν_4 NH bending mode of NH₄⁺, which appears around 1485 cm⁻¹. As more NH₄SH is formed when more NH₃ molecules are available on the sample (exp. iv), the absorbance increases and the band becomes more prominent. Similarly, we detect larger NH₃ signatures (ν_3 near 3370 cm⁻¹ and ν_4 near 1635 cm⁻¹) due to its excess, in the spectrum *a*. Despite a high noise level, mainly caused by the vibrations of the experimental setup and the initial distortion of the baseline, delimited by hatching in Fig. 5, we attribute the 2900–3000 cm⁻¹ absorptions to the NH₄⁺ ion (Ferraro et al. 1980).

As the sample was gradually heated in experiment (iv), we monitored the evolution of the ice with the FT-IR. The main signature of NH₄SH at 1485 cm⁻¹ becomes the sharpest when the temperature of the sample reaches 80 K. This agrees well with the spectrum obtained during the deposition at a constant temperature of 80 K (profile *d*, first phase of exp. vi). Whereas Bragin et al. (1977) find that the salt crystallizes around 100 K, Loeffler et al. (2015) observed amorphous NH₄SH up to 120 K, followed by its crystallization between 130 and 160 K. On the other hand, the crystallization phase of H₂S occurs between 70 and 80 K (Fathe et al. 2006), which corresponds well to the sharp maximum observed under our experimental conditions.

3.3 Salt behaviour under H atoms exposure

To the best of our knowledge, the behaviour of NH₄SH exposed to H atoms has not been studied in the laboratory under conditions relevant to the ISM. Studies on NH₄SH have mainly focused on
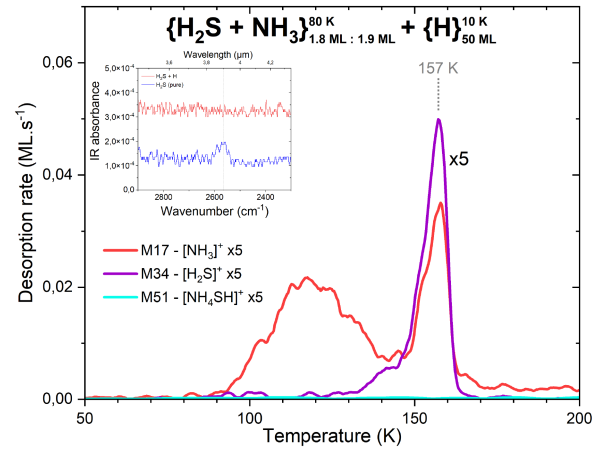

Figure 6. TPD spectra resulting from the {NH₄SH} + {H} experiment (vi). Only the major fragments are shown. Each of them has been multiplied by 5 for readability and scale consistency purposes. *Inset*: infrared spectra of H₂S (bottom curve) and of H₂S + H codeposited (top curve). The grey dashed line shows the absorption band reference (2570 cm⁻¹).

its behaviour in mixed ices (Altwegg et al. 2020), under photolysis (Lebofsky & Fegley 1976), with temperature changes, under proton irradiation (Loeffler et al. 2015, 2016; Loeffler & Hudson 2018), and under electron irradiation (Mahjoub et al. 2016). In contrast, the H-exposure of H₂S has been the subject of some experimental works (Oba et al. 2018; El Akel et al. 2022; Santos, Linnartz & Chuang 2023) and computational studies (Garrod & Herbst 2007; Lamberts & Kästner 2017). In this study, three types of H₂S and NH₄SH H-exposure experiments were performed (Table 1, iii, vi, vii). In all cases, the H atoms flux remained constant at $\phi_H = 8 \times 10^{12}$ atoms cm⁻² s⁻¹.

We found the exposure of H₂S to H atoms to be very effective. With a continuous flow of hydrogen atoms during the deposition, the final amount of product detected in {H₂S + H} corresponds to about 38 per cent of that of a signal of unaltered {H₂S}. However, its infrared signature becomes practically invisible (see inset of Fig. 6), giving us information about the signal-to-noise limit for the detection of H₂S with our RAIRS instrument, which is about 0.25 ML (2.5 × 10¹⁴ molecules cm⁻²). The loss of product can be explained by the chemical desorption that takes place during the reaction processes

$$H_2S + H \longrightarrow HS + H_2, \tag{1}$$

$$HS + H_2 \longrightarrow H_2S + H. \tag{2}$$

According to equation (1) and equation (2), once H₂S undergoes H abstraction to form an HS radical, it is likely to either recombine with another H to reform H₂S or undergo chemical desorption, that is to be ejected be ejected from the surface and return to the gas phase due to excess energy that is too large to dissipate (Dulieu et al. 2013). The competition between the different surface processes, together with the H + H addition, has previously been studied quantitatively (Lamberts & Kästner 2017). The cracking patterns of the residual H₂S remain identical, except for the *m/z* = 35 and 36 which are significantly reduced, possibly indicating a preferential chemical desorption of H₂³⁴S and H³⁴S over H₂³²S.

Exposure of the salt to hydrogen atoms is also effective in reducing the amount of product remaining on the surface, although not as fast as the {H₂S + H} reaction. Fig. 7 shows the time evolution of the infrared band regions of the main NH₄SH signature (at 1485 cm⁻¹) during the experiment (vi). The salt was grown by
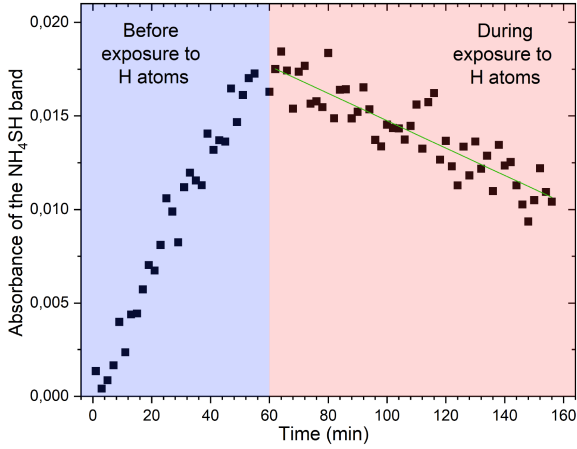
Figure 7. Scatter plot of the infrared band areas of the main signature of NH$_4$SH (1485 cm^{-1}) as a function of time, in the experiment vi. The salt was grown for 60 min at 80 K and then exposed to H atoms for 100 min at 10 K with our atomic beam. The decreasing solid line is a linear fit of the decrease in the IR band area.

one hour {H$_2$S + NH$_3$} codeposition on the surface, which was maintained at 80 K for infrared data readability purposes. We were careful to maintain stable conditions to ensure the lowest possible presence of pure, non-interacting NH$_3$ and H$_2$S on the sample. The surface was then cooled to 10 K before being exposed to hydrogen atoms for 100 min, corresponding to approximately 43 ML of H. The two phases (deposition and H-exposure) are highlighted in Fig. 7 with a blue and red background colour, respectively. We estimate that the salt is destroyed with a half-life of 120 min by sending $\phi_H = 8 \times 10^{12}$ atoms cm^{-2} s^{-1}, which is about 1/3 of the destruction obtained after sending $\sim$ 80 times more hydrogen atoms than the amount of NH$_4$SH present on the surface. It should be noted, however, that this rate of destruction may depend on the intrinsic mobility of H on the surface, which may be slightly different depending on the experimental conditions. In fact, the reformation of H$_2$ consumes most of the H atoms sent to the surface. Here, the destruction of the salt can be fitted with a linear rather than an exponential curve, meaning that the reactivity of the salt can be complete or end with a small plateau. We therefore conclude that, while the salt form does not prevent all hydrogenation or abstraction reactions from occurring, it greatly reduces the reactivity rate, compared to when only molecular H$_2$S is exposed to H.

The TPD traces obtained as a result of this two-phase experiment are shown in the Fig. 6. Each fragment curve has been multiplied by 5, in order to keep the same scale as before. Since there is less NH$_4$SH on the surface, the shift of its desorption temperature from 153 to 157 K is not surprising. As mentioned above, the deposition conditions at 80 K were such that the amounts of pure NH$_3$ and H$_2$S were as low as possible. Despite this, we detect 1.1 ML of excess NH$_3$ as its 'interacting' form after H-exposure, in addition to 0.6 ML of NH$_4^+$ constituting the salt, which gives a total amount of 1.7 ML of residual ammonia on the surface (i.e. $\sim$90 per cent of the total amount of ammonia sent by the beams). An equivalent quantity of 0.55 ML of H$_2$S constituting the salt remains on the sample after sending H atoms (i.e. $\sim$31 per cent of the initial H$_2$S). We also conducted a triple codeposition experiment (vii), in which NH$_3$ molecules, H$_2$S molecules, and hydrogen atoms were simultaneously sent to the surface at 10 K, with fluxes identical to experiment (vi). In contrast to the results of experiment (vi), in experiment (vii) small amounts of pure non-interacting NH$_3$ and H$_2$S remained on the surface (0.2 ML

and 0.1 ML, respectively), in addition to a continuous desorption of NH$_3$ (90–150 K) due to H-bonding (0.85 ML). In this case, between 0.7 and 0.8 ML of each species is incorporated into the salt. Again, it appears that $\sim$95 per cent of NH$_3$ remains on the surface after H-exposure, whereas for H$_2$S it is $\sim$ 46 per cent. The infrared spectrum associated with this experiment is shown in Fig. 5(e). Apart from larger NH$_3$ signatures, no other special features were observed. The small sharp peak at 2342 cm^{-1} corresponds to CO$_2$ due to a minor leak.

Overall, our results show that the consumption of H$_2$S when facing a hydrogen atoms exposure, even in salt form, does occur, but at a reduced rate. The reaction of NH$_4$SH with hydrogen atoms may disrupt the ionic crystal structure of the salt to form NH$_3$+ SH + H$_2$. The process is globally exothermic and is equivalent to the reaction described by reaction 1. In this case, the SH formed could react with the excess of hydrogen atoms to reform H$_2$S, some of which would pass into the gas phase by chemical desorption. This could explain the loss of NH$_4$SH and H$_2$S observed experimentally. However, this reaction does not seem possible because the first step should be NH$_4$SH + H $\longrightarrow$ NH$_3$SH + H$_2$, which is endothermic and should rather form NH$_4$S. In fact, the ionic crystal energy required to form NH$_4$S is similar to that required to form the salt NH$_4$SH:

$$NH_3 + H_2S \longrightarrow NH_4^+ + SH^- (-6.40 \text{ eV}) \tag{3}$$

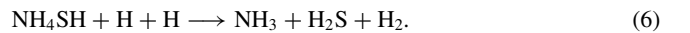$$NH_3 + SH \longrightarrow NH_4^+ + S^- (-6.37 \text{ eV}) \tag{4}$$
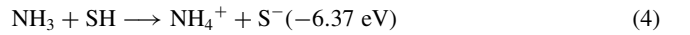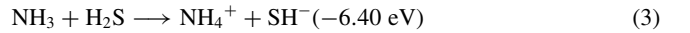
In reaction 4, if there is an excess of hydrogen atoms, NH$_4$SH should be formed, which then acts as a catalyst for the hydrogen recombination reaction (H + H $\longrightarrow$ H$_2$), without loss of H$_2$S by chemical desorption.

Another possibility is the formation of the salt NH$_4$H$_2$S (NH$_4^+$,H$_2$S,e−). With an excess of H, we would then have the following endothermic reaction:

$$NH_4H_2S + H \longrightarrow NH_4^+, H^- + H_2S \longrightarrow NH_3 + H_2S + H_2 \tag{5}$$
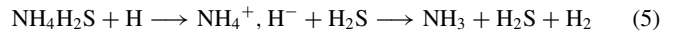
The general reaction would be:

$$NH_4SH + H + H \longrightarrow NH_3 + H_2S + H_2. \tag{6}$$

Some of the H$_2$S formed will give back NH$_4$SH, but some may also react with hydrogen atoms to form H$_2$ + SH and lead to a loss of H$_2$S by chemical desorption during its reformation. It is clear from our results that no pure H$_2$S remains on the surface after 100 min of exposure to H. The fact that NH$_4$SH is less sensitive to hydrogenation than H$_2$S can be explained by the fact that a part of the salt is reformed after reaction with H, while the other part is consumed indirectly by the chemical desorption of H$_2$S according to equation (1), and by the fact that the whole mechanism requires several hydrogen atoms.

Looking at the infrared spectra obtained for this experiment, we observe a progressive destruction of the salt signature at 1485 cm^{-1} during the H-exposure phase. No particular new features were observed, and no quantification of the NH$_3$ reformation could be calculated due to a severe baseline deformation.

3.4 Salt behaviour in water ice mixtures

The behaviour of NH$_4$SH in the environment of other compounds was investigated by Altwegg et al. (2020), who carried out TPD experiments where CH$_3$OH, NH$_3$, H$_2$S, and H$_2$O were simultaneously deposited on a gold-coated surface held at 50 K. They observed the formation of ammonium hydrosulfide in the ice mixture, as in previous works where the use of ^{15}N confirmed the NH$_3$ chemistry
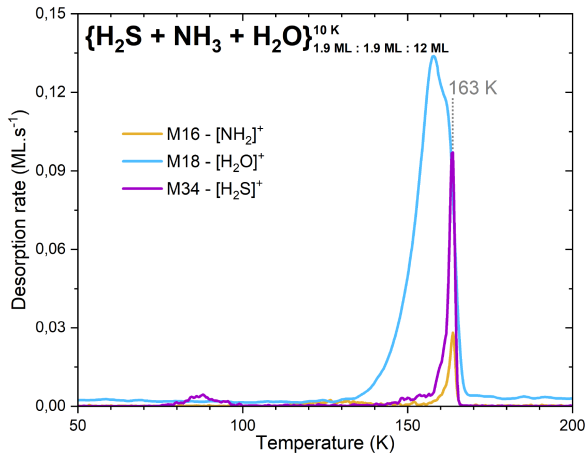
Figure 8. TPD spectra of a H₂S:NH₃:H₂O mixture, where all species have been codeposited at 10 K. The fragment $m/z = 16$ accounts for $[NH_2]^+$, to avoid the confusion between $[NH_3]^+$ and $[OH]^+$ that $m/z = 17$ would result in.

Figure 9. TPD spectra of a H₂S:NH₃:H₂O mixture in more astrnomically relevant conditions. About 1.5 ML of NH₃ and 0.8 ML of H₂S have been deposited bit by bit in a water ice matrix of ∼30 ML. A logarithmic scale is used for readability purposes.

in a similar mixture before its irradiation by electrons and thermal processing (Mahjoub et al. 2016).

Other works have studied more generally the behaviour of ammonium salts in water ice mantles. For example, for salts that desorb at temperatures higher than water ($NH_4^+HCOO^-$, $NH_4^+CH3COO^-$, $NH_4^+CN^-$, among others), no or little influence of H₂O on the TPD profiles of the salts and on the IR spectra has been registered (Noble et al. 2013; Kruczkiewicz et al. 2021). Conversely, for a salt that sublimates in the water desorption region like NH₄SH, we found a shift of 10 K in the desorption temperature, as it can be seen in Fig. 8 which shows the results of experiment (viii). The kinetic order of the desorption does not change, but its maximum appears at the very end of the H₂O desorption, towards 163 K. The NH₄SH binding energy would therefore be greater for H₂O than for gold, implying that even in a codeposition situation, NH₄SH remains bound to water until there is not enough left to hold it on the now too hot surface. We also note that this happens after the water has crystallized.

Given the double assignment of $m/z = 17$ to ionized OH⁺ and NH₃⁺, $m/z = 16$ has been chosen here to represent NH₃. In this experiment, there is no non-interacting NH₃ on the surface; only 0.6 ML of ammonia interacts with either water or NH₄SH. In comparison, 70 per cent and 86 per cent of the total quantity of ammonia and hydrogen sulfide are constituting the NH₄SH salt.

Regarding the infrared results, the major changes undoubtedly concern the water band, located in the absorption regions of NH₃ (3400 cm⁻¹ for the −OH stretching mode and 1650 cm⁻¹ for the H₂O bending mode). Additionally, a slight blue-shift occurs for the H₂S absorption, measured at 2554 cm⁻¹ instead of ∼2570 cm⁻¹ (see Table 2).

In order to verify the influence of a water ice matrix on the desorption of the salt under more astronomically relevant conditions, we performed experiment (ix). The TPD results are displayed in Fig. 9. The IR spectrum is not shown, due to the lack of signal other than H₂O. Approximately 0.8 ML of H₂S and 1.5 ML of NH₃ have been diluted in 30 ML of H₂O at 10 K, as a result of regular valve openings throughout the deposition. The readability of the results is therefore improved by using a logarithmic scale and dividing the H₂O component by a factor of 10. As in experiment (viii), very small returns from NH₄SH to H₂S and NH₃ are visible (0.1 ML of each, approximately). The desorption is also shifted to 163 K, following the same pattern as the end of the water desorption. Our results are
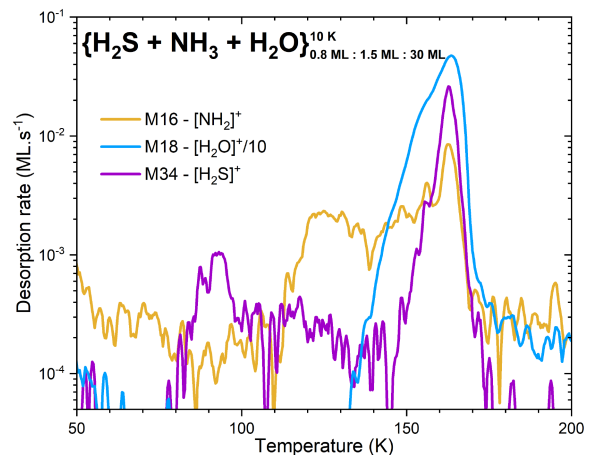
consistent with the single NH₄SH TPD spectrum published to date, where the desorption peak occurs at 168 K in a mixed ice containing H₂O, CH₃OH, H₂S, and NH₃ (Altwegg et al. 2020).

Overall, water seems to affect the desorption and decomposition of NH₄SH only by delaying it, shifting its temperature by 10 K under our experimental conditions, regardless of the mixture ratios between different species.

4 ASTROPHYSICAL IMPLICATIONS

H₂S and OCS are the main sulphur species observed in the gas phase in protostars (Kushwahaa et al. 2023), with variable ratios. It is therefore important to understand the evolution of their ratios through modelling, as well as the potential role of salts that form when *s*-H₂S (*s*- meaning solid, on surfaces) is mobile on ice, during a temperature increase. To model the abundances in protostars, we used the Nautilus gas–grain model in its three-phase form (Ruaud, Wakelam & Hersant 2016). The model was used to simulate the abundances of atoms and molecules in neutral and ionic form as a function of time, employing kida.uva.2014 (Wakelam et al. 2015). The basic chemical network has recently been updated to better describe COMs on grains and in the gas phase (Manigand et al. 2021; Loison et al. 2022; Agúndez et al. 2023), but also to describe the formation of salts. 800 species are identified in the network and are involved in 9000 individual reactions. In the model that we used, the elements are initially in their atomic or ionic form (the ones with an ionization potential below 13.6 eV are considered to be fully ionized), and the C/O elemental ratio is equal to 0.71. The initial sulphur abundance is set to 6.0×10^{-7} with respect to H, corresponding to a depletion by a factor of 20 compared to the typical cosmic abundance in dense molecular clouds (Fuente et al. 2016). The grain surface and the mantle are both chemically active in these simulations, while the accretion and desorption processes are allowed only between the surface and the gas phase, except for the sputtering by cosmic rays. The dust-to-gas ratio is 0.01 by mass. A sticking probability of 1 is assumed for all neutral species, and desorption can occur via thermal and non-thermal processes, including chemical desorption and sputtering of ices by cosmic ray collisions (Wakelam et al. 2021). The formalism of the surface reactions and a more
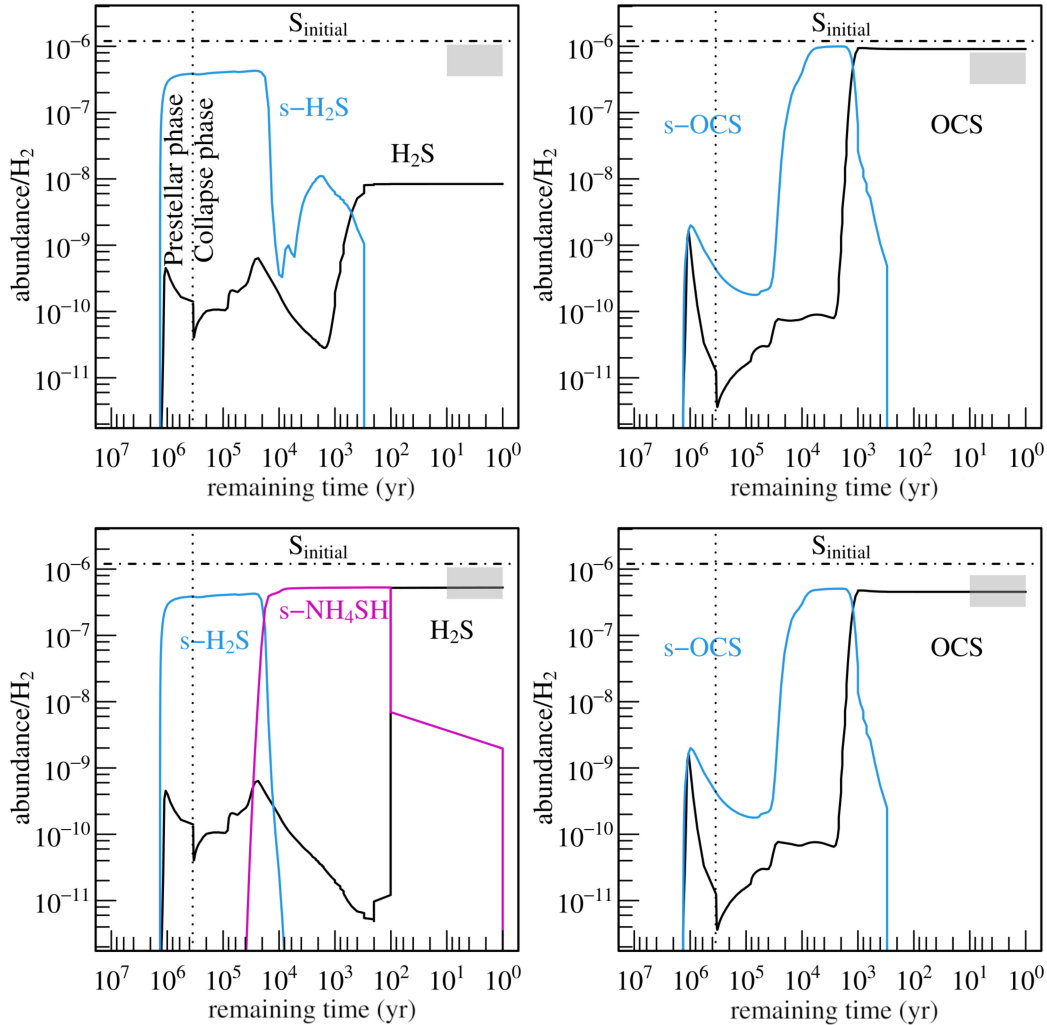
Figure 10. Fractional abundances (n/n_{H_2}) of H_2S, and NH_4SH (left panels) and OCS (right panels) in gas phase (black lines) and on the grain surface (blue and purple lines) as a function of time during the collapse phase predicted by the Nautilus astrochemical model. The time axis is reversed to better visualize the abundance evolution. Upper panels: without NH_4SH formation pathway. Lower panels: with inclusion of NH_4SH formation pathway. The abundance of sulphur initially in the gas phase is fixed at 1.2×10^{-6}, that is a depletion factor of 20 compared to the solar abundance (Asplund et al. 2009). The grey rectangle at the top right of each pannel represents the observed abundances towards IRAS 16293−2422B (Kushwahaa et al. 2023), assuming an uncertainty of 3×10^{-7} in the *y*-axis.

detailed description of the simulations can be found in Ruaud et al. (2016).

To study the chemistry in protostellar envelopes, we have used the same approach as in Manigand et al. (2021). We perform two steps: a prestellar and a collapse phase. In the first step, conditions typical of the cold core are assumed for 10^6 yr (gas and dust temperature of 10 K, a proton density of 2×10^4 cm^{-3}, a visual extinction of 4.5 mag, a cosmic ray ionization rate of 1.3×10^{-17} s^{-1}, and a standard external UV field of 1 G0). The final composition of the cold core is then used as the initial condition for the collapse phase, which is the same as in Aikawa et al. (2008, 2012), Wakelam et al. (2014), and Manigand et al. (2021). The selected parcel of gas begins to collapse at a radius of about 10 000 au and ends-up at a radius of 15 au, where the gas temperature reaches ∼265 K and a density of 4×10^8 cm^{-3}.

In the version of the NAUTILUS code used in this work, we have introduced two types of salts: salts stable in the gas phase and ammonium salts, that would form by the Langmuir–Hinshelwood

mechanism. The former, such as table salt Na$^+$Cl$^-$, can be considered as classical molecules, even if they dissociate as ions in ice (Acharyya, Woon & Herbst 2023). On the other hand, ammonium salts do not exist in the gas phase and are only stable when the ions resulting from a proton transfer from an acid to the base (here, ammonia) are sufficiently stabilized by interactions with water molecules, in order to compensate for the exothermicity of the proton transfer. Calculating the interaction energy between ions and the structure of amorphous ices is therefore very complicated, as it is necessary to estimate for which systems these energies are sufficient to ensure the formation of ion pairs, that is salts. To do this, we have used a method similar to that of Woon (2012), which consists in calculating the most stable structures for acid-base-(H2O)$_n$ systems by varying the size of the water cluster. If a proton transfer occurs for $n \leq 8$, we consider the salt formation, barrierless when exothermic (Woon 2012). The ammonium salts thus introduced are NH$_4^+$CN$^-$, NH$_4^+$Cl$^-$, NH$_4^+$NCO$^-$, NH$_4^+$NCS$^-$, NH$_4^+$HCOO$^-$, and NH$_4^+$SH$^-$. This would explain, among other things, the ice

absorption band usually observed at $2165\,cm^{-1}$ $(4.62\,\mu m)$ and attributed to OCN^-. However, since the bands attributed to OCN^- and NH_4^+ are seen in dense molecular cloud ices (McClure et al. 2023), it also implies that either NH_3, HNCO, or HOCN are mobile at low temperatures, so that the diffusion energy is much lower than the usual value of 0.4 times the adsorption energy.

In this first version of the NAUTILUS code with salts taken into account, and despite our experimental results showing a significant reactivity, even reduced, of salts with hydrogen atoms, we do not include salt destruction reactions except for desorption. Due to the instability of ammonium salts in the gas phase, unlike usual molecules, we cannot calculate their desorption temperature with the usual models, including the proxy approach developed in Wakelam et al. (2017). We have therefore chosen to set the desorption energies for the destructive process s-$NH_4SH \rightarrow NH_3 + H_2S$ so as to reproduce the experimental sublimation temperature of about 150 K for s-NH_4SH, corresponding to a binding energy of about 6000 K, slightly larger than that of water.

In models of ice formation in interstellar clouds, the gas-phase reactions of S^+ and S are not efficient enough to consume significant amounts of sulphur, which will eventually stick to the ice. The evolution of solid sulphur at low temperatures in dense clouds (around 10 K) is then dominated by reactions with atomic hydrogen, with the production of s-H_2S. As the H–SH bond of H_2S is weaker than the H–H bond of H_2, s-H_2S tends to react with s-H by tunneling effect, giving s-H_2 + s-SH. The s-SH radical can also react with s-H to give mainly s-H_2S (and probably s-S), creating a loop and thus an equilibrium between s-H_2S and s-SH (and s-S) (Lamberts & Kästner 2017; Vidal et al. 2017; Oba et al. 2018). Since both s-SH and s-H_2S have similar abundances at 10 K in our model and are the main reservoir of sulphur for evolved dense clouds, this equilibrium is controlled by the abundance and mobility of H on the gains.

The resulting model predictions are shown in Fig. 10. Inclusion of the experimental results in the NAUTILUS astrochemical gas–grain model corroborates the importance of solid-state NH_4SH to better constrain the H_2S and OCS abundances (Fig. 10, lower panels). When the dense cloud gives rise to the formation of protostars, the temperature in the collapse phase increases, leading to a significant increase in the mobilities of the various species present on the grains, especially radicals. Among the radicals we count s-SH and s-S, but also s-HCO, i.e. the most abundant radical on the grains due to that of s-CO, together with notable abundances of s-CH_2OH and s-CH_3O. In our model, the mobilities of s-SH, s-S, and s-HCO are comparable and inferred from the adsorption energies of Wakelam et al. (2017). The reaction of s-S with s-HCO gives s-SH + s-CO as well as s-H + s-OCS, while the reaction of s-SH and s-HCO can give s-HCOSH, s-H_2S + s-CO, and s-H_2 + s-OCS. The solid s-HCOSH species reacts quite easily with H by tunneling effect and are converted fairly rapidly to s-OCS. HCOSH was detected towards quiescent clouds in the Galactic Centre (Rodríguez-Almeida et al. 2021; García de la Concepción et al. 2022), which is in good agreement with our model, where the abundance of s-HCOSH in protostars is low.

5 CONCLUSIONS

In our experimental study, we took a closer look at the formation, reactivity, and desorption of ammonium hydrosulfide salts. These salts are in fact chemical intermediates with specific properties that give them an important role in molecular evolution during star formation processes, but also in the sublimation of ices in general, as in comets. In particular, we have shown that:

(i) NH_4SH salts are formed at temperatures as low 10 K from a mixture of H_2S and NH_3, and appear to crystallize around 80 K under our experimental conditions.

(ii) Even diluted in water, H_2S, and NH_3 mixtures lead to the formation of ammonium hydrosulfide salts, and their desorption is shifted to 163 K, that is 10 K higher than in the H_2S:NH_3 case, regardless of the mixture ratios in the H_2O:H_2S:NH_3 system.

(iii) In astrophysical contexts (i.e. protostars or protostellar discs), salts are likely to desorb with water, and in any case at higher temperatures than the individual pure species NH_3 and H_2S.

(iv) Adopting an effective binding energy of $\sim$6000 K for NH_4SH and the release of the two components NH_3 and H_2S in the gas phase seems a reasonable description of the desorption process.

(v) Including salts in present chemical networks helps to find a better agreement with the observed OCS/H_2S ratio in protostars.

(vi) S-bearing ionic compounds could explain the non-detection of H_2S in ices to date, as some of it would be in the form of salts.

(vii) Salts do not provide total protection of H_2S against exposure to hydrogen atoms, but they do slow down the H-abstraction process.

DATA AVAILABILITY

The experimental data and conditions have been saved on our own laboratory server, under the form of metadata files associated with each experiment. They will be released publicly after a minimum of 3 yr after their production. For the time being, the data are available from the corresponding authors upon reasonable request.

REFERENCES

Acharyya K., Woon D. E., Herbst E., 2023, MNRAS, 527, 1722
Agúndez M. et al., 2023, A&A, 673, A34
Aikawa Y., Wakelam V., Garrod R. T., Herbst E., 2008, ApJ, 674, 984
Aikawa Y., Wakelam V., Hersant F., Garrod R. T., Herbst E., 2012, ApJ, 760, 40
Altwegg K. et al., 2020, Nat. Astron., 4, 533
Asplund M., Grevesse N., Sauval A. J., Scott P., 2009, ARA&A, 47, 481
Atreya S. K., Wong M. H., Owen T. C., Mahaffy P. R., Niemann H. B., Pater I. D., Drossart P., Encrenaz T., 1999, Planet. Space Sci., 47, 1243
Bergner J. B., Öberg K. I., Rajappan M., Fayolle E. C., 2016, ApJ, 829, 85
Bouilloud M., Fray N., Bénilan Y., Cottin H., Gazeau M.-C., Jolly A., 2015, MNRAS, 451, 2145
Bragin J., Diem M., Guthals D., Chang S., 1977, J. Chem. Phys., 67, 1247
Van Broekhuizen F. A., Keane J. V., Schutte W. A., 2004, A&A, 415, 425
Calmonte U. et al., 2016, MNRAS, 462, S253
Chen Y. J. et al., 2015, ApJ, 798, 80
Clutter D. R., Thompson W. E., 1969, J. Chem. Phys., 51, 153
Congiu E. et al., 2012, ApJ, 750, L12
Congiu E., Sow A., Nguyen T., Baouche S., Dulieu F., 2020, Rev. Sci. Instrum., 91, 124504
Demyk K., Dartois E., D'Hendecourt L., Muizon M. J. D., Heras A. M., Breitfellner M., 1998, A&A, 339, 553
Drozdovskaya M. N. et al., 2018, MNRAS, 476, 4949
Dulieu F., Congiu E., Noble J., Baouche S., Chaabouni H., Moudens A., Minissale M., Cazaux S., 2013, Sci. Rep., 3, 1338

El Akel M., Kristensen L. E., Gal R. L., Van Der Walt S. J., Pitts R. L., Dulieu F., 2022, A&A, 659, A100

Fathe K., Holt J. S., Oxley S. P., Pursell C. J., 2006, J. Phys. Chem. A, 110, 10793

Ferrante R. H., Moore M. H., Spiliotis M. M., Hudson R. L., 2008, ApJ, 684, 1210

Ferraro J. R., Sill G., Fink U., 1980, Appl. Spectrosc., 34, 525

Filacchione G. et al., 2019, Space Sci. Rev., 215, 19

Friedson A. J., 2005, Icarus, 177, 1

Fuente A. et al., 2016, A&A, 593, A94

Gálvez O., Maté B., Herrero V. J., Escribano R., 2010, ApJ, 724, 539

García de la Concepción J. et al., 2022, A&A, 658, A150

Garrod R. T., Herbst E., 2007, A&A, 467, 1103

Gerakines P. A., Moore M. H., Hudson R. L., 2004, Icarus, 170, 202

Gerakines P. A., Yarnall Y. Y., Hudson R. L., 2024, Icarus, 413, 116007

Goicoechea J. R., Pety J., Gerin M., Teyssier D., Roueff E., Hily-Blant P., Baek S., 2006, A&A, 456, 565

d'Hedencourt L. B., Allamandola L. J., 1986, A&AS, 64, 453

Hudgins D. M., Sandford S. A., Allamandola L. J., Tielens A. G. G. M., 1993, ApJS, 86, 713

Hudson R. L., Gerakines P. A., 2018, ApJ, 867, 138

Jiménez-Escobar A., Caro G. M. M., Chen Y. J., 2014, MNRAS, 443, 343

Kruczkiewicz F., Vitorino J., Congiu E., Theulé P., Dulieu F., 2021, A&A, 686, A236

Kumar Y., Kumar M., 2020, Chem. Phys. Lett., 740, 137071

Kushwahaa T., Drozdovskaya M. N., Tychoniec L., Tabone B., 2023, A&A, 672, A122

Lamberts T., Kästner J., 2017, J. Phys. Chem. A, 121, 9736

Lebofsky L., Fegley M., 1976, Icarus, 28, 379

Li C. et al., 2020, Nat. Astron., 4, 609

Lodders K., 2010, Solar System Abundances of the Elements, Astrophysics and Space Science Proceedings. Springer-Verlag, Berlin

Loeffler M. J., Hudson R. L., 2018, Icarus, 302, 418

Loeffler M. J., Hudson R. L., Chanover N. J., Simon A. A., 2015, Icarus, 258, 181

Loeffler M. J., Hudson R. L., Chanover N. J., Simon A. A., 2016, Icarus, 271, 265

Loison A. C. J.-C., Boulanger A., Caux E., Müller H. S. P., Wakelam V., Manigand S., Jørgensen J. K., 2022, A&A, 660, L6

López-Gallifa Á. et al., 2024, MNRAS, 529, 3244

Mahjoub A. et al., 2016, ApJ, 820, 141

Manigand S. et al., 2021, A&A, 645, A53

Martín-Doménech R., Jiménez-Serra I., Caro G. M. M., Müller H. S., Occhiogrosso A., Testi L., Woods P. M., Viti S., 2016, A&A, 585, A112

McClure M. K. et al., 2023, Nat. Astron., 7, 431

Niemann H. B. et al., 1998, J. Geophys. Res.: Planets, 103, 22831

Noble J. A., Dulieu F., Congiu E., Fraser H. J., 2011, ApJ, 735, 121

Noble J. A., Theule P., Borget F., Danger G., Chomat M., Duvernay F., Mispelaer F., Chiavassa T., 2013, MNRAS, 428, 3262

Oba Y., Tomaru T., Lamberts T., Kouchi A., Watanabe N., 2018, Nat. Astron., 2, 228

Pater I. D., Dunn D., Romani P., Zahnle K., 2001, Icarus, 149, 66

Perrero J., Beitia-Antero L., Fuente A., Ugliengo P., Rimola A., 2024, MNRAS, 527, 10697

Phuong N. et al., 2018, A&A, 616, L5

Raunier S., Chiavassa T., Marinelli F., Allouche A., Aycard J. P., 2003, Chem. Phys. Lett., 368, 594

Rodríguez-Almeida L. F. et al., 2021, ApJ, 912, L11

Roman M. T., Banfield D., Gierasch P. J., 2013, Icarus, 225, 93

Ruaud M., Wakelam V., Hersant F., 2016, MNRAS, 459, 3756

Ruffle D. P., Hartquist T. W., Caselli P., Williams D. A., 1999, MNRAS, 306, 691

Santos J. C., Linnartz H., Chuang K.-J., 2023, A&A, 678, A112

Savage B. D., Sembach K. R., 1996, ApJ, 470, 893

Smith R. G., 1991, MNRAS, 249, 172

Suresh S. K., Dulieu F., Vitorino J., Caselli P., 2024, A&A, 682, A163

Theulé P., Duvernay F., Danger G., Borget F., Bossa J. B., Vinogradoff V., Mispelaer F., Chiavassa T., 2013, Adv. Space Res., 52, 1567

Tieftrunk A., des Forets G. P., Schilke P., Walmsley C. M., 1994, A&A, 289, 579

Vidal T. H. G., Loison J.-C., Jaziri A. Y., Ruaud M., Gratier P., Wakelam V., 2017, MNRAS, 469, 435

Vinodkumar M., Bhutadia H., Limbachiya C., Joshipura K. N., 2011, Int. J. Mass Spectrom., 308, 35

Wakelam V., Vastel C., Aikawa Y., Coutens A., Bottinelli S., Caux E., 2014, MNRAS, 445, 2854

Wakelam V. et al., 2015, ApJS, 217, 20

Wakelam V., Loison J. C., Mereau R., Ruaud M., 2017, Mol. Astrophys., 6, 22

Wakelam V., Dartois E., Chabot M., Spezzano S., Navarro-Almaida D., Loison J.-C., Fuente A., 2021, A&A, 652, A63

Weidenschilling S. J., Lewis J. S., 1973, Icarus, 20, 465

Wong M. H., Mahaffy P. R., Atreya S. K., Niemann H. B., Owen T. C., 2004, Icarus, 171, 153

Woon D. E., 2012, Comput. Theor. Chem., 984, 108

This paper has been typeset from a TEX/LATEX file prepared by the author.